Research Paper

# UV and visible hydrogen photo-production using Pt promoted Nb-doped TiO$_2$ photo-catalysts: Interpreting quantum efficiency

Olga Fontelles-Carceller, Mario J. Muñoz-Batista, José Carlos Conesa, Marcos Fernández-García*, Anna Kubacka*

*Instituto de Catálisis y Petroleoquímica, CSIC, C/ Marie Curie, 2. 28049 Madrid, Spain*

## ARTICLE INFO

## ABSTRACT

Nb-doped titania nanopowders active under UV and visible light were used as supports of platinum and tested in the photo-production of hydrogen using methanol as sacrificial agent in liquid phase. Samples were characterized using X-ray diffraction and photoelectron spectroscopy, UV–vis and photo-luminescence spectroscopies, electron paramagnetic resonance, and transmission electron microscopy. The catalytic performance was evaluated taking into account the measurement of the corresponding reaction rates and the computation of the quantum efficiency values. Optimization of the catalytic output upon UV and visible excitation was carried out as a function of the Nb content of the material and using an experimental design taking as factors the methanol:water ratio, and catalyst concentration at liquid phase. The performance of the materials and the optimum for a catalyst containing a 2.5 mol% of Nb upon UV, visible light and sunlight was examined. The characterization results concerning both the charge carrier species recombination and the fate of such species at the catalytic surface were used to elucidate the physico-chemical roots for maximizing activity.

© 2017 Elsevier B.V. All rights reserved.

## 1. Introduction

Hydrogen appears as an energy vector essential for achieving a sustainable and greener future. This is due to the fact that the molecule is ideal to store energy (ca. 3 times more than conventional natural gas per unit volume) and does not generate toxic or dangerous molecules during its chemical transformation to release energy [1]. Production of hydrogen using light and bio-derived molecules trough photocatalysis can provide a sustainable and attractive path with neutral carbon emissions, contributing to the above mentioned greener future [2–7]. Several bio-alcohols have been tested in such a process, those having at least one hydrogen atom bonded to the (carbon) alpha position being the ones rendering higher reaction rates [8–24]. Among those, methanol is the simplest molecule from the structural and chemical points of view and probably the molecule receiving most attention due to the relatively high hydrogen production rates commonly observed with it [25–28].

Titania-based materials have customarily been used in photo-catalysis due to a number of properties including their relatively

low cost, high availability, and significant activity in all reactions tested. Outstanding activity of titania-based catalysts has been reported in the production of hydrogen from water resources using bio-alcohols as sacrificial agents [2–7,29]. In photochemical and more frequently in photoelectrochemical processes, doping of titania with Nb has been used to enhance charge transport and mobility, particularly concerning electron-related species [30,31]. This aspect is potentially important in the hydrogen production process, which requires as a primary step the reduction of protons with electrons to drive the formation of the hydrogen molecule. Moreover, Nb-doped titania photocatalysts have shown notable activity under visible light, opening a way to achieve optimum profit of sunlight and thus to render a fully sustainable chemical process for hydrogen photo-production [32–39].

In the photocatalytic production of hydrogen using titania based materials, the use of a metallic co-catalyst has been shown to boost activity significantly [2,6,40,41]. Platinum is the most studied noble metal co-catalyst to this aim due to the exceptional performance showed under all illumination and conditions tested. Pt has the highest work function among noble metals, and would thus drive a stronger electron transfer from titania, and displays the lowest activation energy for proton reduction. These two facts would make it a reasonable choice for the photo-generation of hydrogen [42]. Acording to previous works, Pt (and other noble metals) promotion of photo-activity has its roots in a significant number of physico-

* Corresponding authors.
*E-mail addresses:* mfg@icp.csic.es, m.fernandez@icp.csic.es
(M. Fernández-García), ak@icp.csic.es (A. Kubacka).

chemical phenomena including those related to morphology as e.g. primary particle size, shape, interface contact with the anatase and electron transfer-related (charge separation and handling) properties between the metal and the oxide, as well as electron-acceptor properties of the metal phase itself and subsequent beneficial effects in charge recombination [16,18,26–28,43–56].

In this work we use a 0.5 wt.% Pt promotion of Nb-doped titania samples, which are prepared by microemulsion followed by Pt deposition using a chemical reduction method. The oxide preparation process ensures the obtention of substitutional mixed oxide phases (Nb located at cation positions of the dominant phase) of titania materials [33,34]. We carried out the study of photocatalytic hydrogen production under different illumination sources, with particular emphasis in the use of UV and visible illumination conditions. The study aims to provide information in connection with the fruitful use of sunlight for this photochemical process [26,54,56]. To report an analysis of the photocatalytic properties on rigorous basis, a full calculation of the quantum efficiency is mandatory. The later requires the analysis of the optical properties of the catalyst at a liquid media as well as the use of up to date numerical analysis procedures to render accurate (also called "true" in opposition to the "apparent") values of the efficiency [57–62]. We interpret the quantum efficiency behavior through the series with the help of photoluminescence and electron paramagnetic resonance data concerning the fate of the charge carrier species as well as their transformation into radical species interacting with the sacrificial agent (holes) and protons (electrons) leading to hydrogen molecule.

## 2. Material and methods

### 2.1. Preparation and characterization of catalysts

Materials were prepared using a microemulsion method by addition of Titanium tetraisopropoxide to an inverse emulsion containing an aqueous solution of hydrated niobium nitrate (Sigma) dispersed in $n$-heptane, using Triton X-100 (Aldrich) as surfactant and hexanol as cosurfactant. Total cation content of the aqueous solution is 0.5 M. Water/(Ti + Nb) and water/surfactant molar ratios were, respectively, 18 and 110 for all samples. The resulting mixture was stirred for 24 h, centrifuged, decanted, rinsed with methanol and dried at 300 K for 6 h. Following the microemulsion preparation method, the amorphous Nb-Ti powders were calcined under air for 2 h at 723 K. The co-catalyst was introduced subsequenty by a chemical deposition method using a $H_2PtCl_6$ (Aldrich) solution. First, the Nb-Ti powder was suspended by stirring in a deionized water solution for 30 min. After that, the proper quantity of $H_2PtCl_6$ was subsequently added to the solution (to get a 0.5 wt.% of Pt on metal basis) and kept under stirring 5 min more. The reduction was carried out using a $NaBH_4$ (Aldrich) aqueous solution ($Pt/NaBH_4$ molar ratio 1/5). The final solid was rinsed with deionized water, collected by centrifugation and dried at 353 K.

Samples are named xNbTi/Pt with x indicating the molar fraction of Nb on cationic basis in the titania component. Nb and Pt content of the solids were measured with total reflection x-ray fluorescence (Bruker − S2 PicoFox TXRF Spectrometer) rendering values equal to the nominals ones within an error below 2.9 and 2.1% for, respectively, Nb and Pt components.

XRD profiles of the samples were obtained using a polycrystal XíPert Pro PANalytical diffractometer using Ni-filtered Cu Kα radiation with a 0.02° step. Crystallite sizes reported were calculated from XRD patterns using the Williamson-Hall method which takes into account the strain and particle size contributions to the XRD peak broadening [63]. Raman data were acquired using a Renishaw Dispersive system 1000, equipped with a single monochromator, a holographic Notch filter, and a cooled TCD.

Samples were excited using the 514 nm Ar line. The BET surface areas and average pore sizes and pore volumes were measured by nitrogen physisorption (Micromeritics ASAP 2010). UV−vis diffuse-reflectance spectroscopy experiments were performed on a Shimadzu UV2100 apparatus using $BaSO_4$ or Teflon as a reference, and the results presented as Kubelka-Munk transform [64]. Band gap analysis for an indirect/direct semiconductor was done following standard procedures; e.g. plotting $(hva)^n$ ($n = ½$ or 2 for indirect or direct semiconductor; $hv$ = excitation energy, $a$ = absorption coefficient, assumed to be proportional to the Kubelka-Munk transform in the relevant wavelength range) vs. energy and obtaining the corresponding intersection of the linear fit with the baseline [65]. Photoluminescence spectra were measured at room temperature on a Fluorescence Spectrophotometer (Perkin Elmer LS50B). Transmission electron microscopy (HTEM) and X-ray energy dispersive spectra (XEDS) were recorded on a JEOL 2100F TEM/STEM microscope. Particle size distributions of the noble metal were obtained counting more than 150 particles in all cases.

XPS spectra were obtained with a SPECS spectrometer, with main chamber working at a pressure <$10^{-9}$ Torr and equipped with a PHOIBOS 150 multichannel hemispherical electron analyser and a dual X-ray source working with Ag Kα ($hv$ = 1486.2 eV) at 120 W, 20 mA; energy calibration used the C(1s) peak of adventitious carbon as energy reference (284.6 eV). The spectra were recorded on $4 \times 4 mm^2$ pellets, 0.5 mm thick, prepared by slightly pressing the powered materials, which were outgassed in the prechamber of the instrument at room temperature up to a pressure <$2 \times 10^{-8}$ Torr to remove chemisorbed water from their surfaces. Surface chemical compositions were estimated from XP-spectra, by calculating the integral of each peak after subtraction of the "S-shaped" Shirley-type background [66] using the appropriate experimental sensitivity factors and the CASA-XPS (version 2.3.15) software. For the study of the Pt $4f$ signal of the Pt-containing solids, the background at the Pt $4f$ region of the titania support (Ti $3s$ plasmon loss) was subtracted.

The electron paramagnetic resonance (EPR) measurements were done with a Bruker ER200D spectrometer operating in the X-band and calibrated with a DPPH standard. For the 5,5-dimethyl-1-pyrroline N-oxide (DMPO) spin trapping EPR experiments, the samples were suspended in water or methanol (at a concentration of $0.5 g L^{-1}$) and were sonicated for 4 min. A solution (0.01 M) of DMPO spin trap (supplied by Sigma) was prepared and kept on ice during the whole set of experiments. Bidistilled water (Elix-10) or methanol (Sigma) were employed for these preparations. 100 μL of the solid suspension and 100 μL of the DMPO solution were mixed into an EPR flat quartz cell under atmospheric air and irradiated at different times, through a spectroscopic Pyrex glass filter with a cut-off at ca. 290 nm, with light excitation source identical to that employed for the photocatalytic tests, being then immediately transferred to the spectrometer cavity for EPR analysis. A small radical concentration decay (of ca. 3.5% on average) was observed in the dark during the course of spectrum recording. Spectra were recorded at 298 K at ca. 9.75 GHz microwave frequency, 19.5 mW microwave power, 100 kHz modulation frequency, 1 G modulation amplitude and $2 \times 10^5$ spectrometer gain. No significant signal saturation was observed in those conditions. Blank experiments were also performed over mixtures of 100 μL of the DMPO solution and 100 μL of water or methanol to check the absence of radical formation in the absence of solid under the employed conditions.

### 2.2. Description of reactor

Photocatalytic measurements at liquid medium were carried out using a batch pyrex (cutting absorption edge at ca. 300 nm) reactor of 4 cm depth depicted in Fig. 1. The reactor is filled with ca. 50 mL of a suspension of the catalyst in a x:y (x:y from 1:9 to
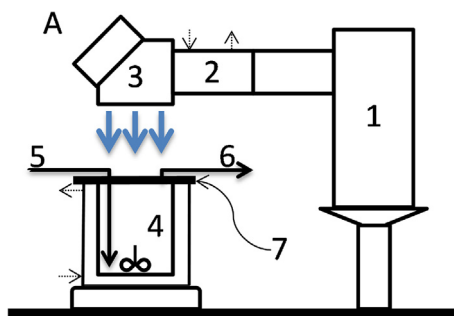
**Fig. 1.** Schematic representation of the experimental photoreactor: (1) Hg-Xe lamp, (2) Water filter, (3) dichroic filter (280–400 nm or 420–680 nm), (4) Methanol-water/catalyst suspension, (5) Argon carrier inlet, (6) Argon carrier and gas products outlet, and (7) neutral filter. Dotted arrows indicate inlet and outlet cooling water.

9:1 v/v) MeOH/$H_2O$ mixture medium maintained at a constant temperature (293 ± 1 K). The catalyst suspension (0.25–1.0 g $L^{-1}$) was first degassed with an Ar stream for around 20 min. Unless explicitly mentioned in the text, the standard catalyst concentration was 0.5 g $L^{-1}$. This concentration was selected as representative for conditions optimizing activity output based on a preliminary reaction test carried out using all illumination sources of the study (see Fig. S1 at supporting information). Subsequently, the Ar flow was settled down to 10 mL $min^{-1}$ and stabilized before reaction. Ar is used as carrier to transport the reaction-produced gases from the reactor to the detection system. The solution in the reactor was irradiated using a Hg-Xe lamp (500 W) and dichroic filters (all form LOT-Quantum Design) allowing exposure of the catalysis to either the UV (280–400 nm) or Visible (420–680 nm) wavelength ranges. The reaction rates were evaluated at 3 h from the start of the irradiation, where a pseudo-stationary situation is reached for the gas-phase production of hydrogen.

Hydrogen production rate was analyzed using an on-line Mass spectrometry (Onmistart 300), gas chromatography (with TCD/FID detection using HP-PLOT/Innowax columns in an Agilent 6890 apparatus) and liquid chromatography (xD8-C18/5 microm, 4.6 × 150 mm Agilent HPLC Column Eclipse and a Varian Pro Star 230 apparatus).

### 2.3. Quantum efficiency evaluation

This evaluation depends on a precise determination of the average volumetric rate of photon absorption, which was obtained here, following a literature method [67], by solving numerically the Radiative Transfer Equation (RTE) in the reactor system schematically presented in Fig. 1. The RTE determines the variation of intensity $I_{\lambda,\Omega}$ (associated to a light beam with wavelength $\lambda$ in the direction of a solid angle vector, $\underline{\Omega}$) through a direction of the space (s) by means of Equation (1) (the symbols in the equation, and in all the rest of the text, are listed in the Supporting Information section). The equation assumes; (i) that the emission of radiation by the solution is negligible (at room temperature), and (ii) that a steady state condition is reached during the photocatalytic processes.

$$\frac{dI_{\lambda,\underline{\Omega}}(\underline{x})}{ds} = -\kappa_\lambda(\underline{x})I_{\lambda,\underline{\Omega}}(\underline{x}) - \sigma_\lambda(\underline{x})I_{\lambda,\underline{\Omega}}(\underline{x})$$

$$+ \frac{\sigma_\lambda(\underline{x})}{4\pi} \int_{\Omega'=4\pi} p\left(\underline{\Omega}' \to \underline{\Omega}\right) I_{\lambda,\underline{\Omega}'} d\underline{\Omega} \tag{1}$$

#### 2.3.1. Determination of optical properties

To solve equation 1 it is necessary to determine, first, the optical properties of the photocatalysts suspensions (obtained in the

adequate etanol:water mixture and under agitation in conditions approaching the ones at the reactor). These are the spectral absorption coefficient ($\kappa_\lambda$), the spectral scattering coefficient ($\sigma_\lambda$), and the scattering phase function ($p\left(\underline{\Omega}' \to \underline{\Omega}\right)$). To do it, the extinction coefficient of the samples ($\beta_\lambda = \sigma_\lambda + k_\lambda$) was experimentally obtained by applying a standard linear regression to the plots of $\beta_\lambda$ (range 200–680 nm) versus catalyst concentration C. Six concentrations ($5 \times 10^{-2}$–1.5 g $L^{-1}$) were used to calculate the extinction coefficient as $\beta_\lambda = 2.303ABS_\lambda/L$; where L represented the cell path length. The specific extinction coefficient $\beta_\lambda^*$ is the slope of the $\beta_\lambda$, C linear fit. The measurements were carried out using 0.1–0.5 cm cuvettes and narrow vertical slits; i) before the sample to ensure beam homogeneity, and ii) after the sample to minimize scattered radiation from the cell itself. To obtain the scattering phase function, and according with previous studies in similar $TiO_2$-based catalysts, the Henyey and Greenstein phase function (Equation (2)) was adopted [68].

$$p\left(\underline{\Omega}' \to \underline{\Omega}\right) = \frac{1 - g_\lambda^2}{\left(1 + g_\lambda^2 - 2g_\lambda^2 u_0\right)^{3/2}} \tag{2}$$

In Eq. (2) $g_\lambda$ is the so-called asymmetry factor and $u_0$ is the director cosine between incoming and outgoing light at each point of the space.

The optical properties were obtained by solving the RTE (which considers radiation absorption and scattering effect by the catalyst; Eq. (1)), using the discrete ordinate method (DOM), for a rectangular, spectrophotometer cell in combination with a nonlinear, multiparameter regression procedure (lsqnonlin, Algorithm: Trust-Region-Reflective Optimization; MATLAB 2012b). The cell path (1–2 mm) was selected to provide "stable" optical parameters. This cell dimension allows to representing the cell as an infinite plane parallel medium with azimuthal symmetry, a one-dimensional, one-directional radiation transport model can be used to solve the RTE (see Fig. S2A at the supporting information section) [67,69].

Fig. S2A thus shows a schematic representation of the spectrophotometer cell and the corresponding RTE solution scheme where the net light intensity is represented by one angular-dependent variable ($\mu = \cos(\theta)$) defined at each point of the cell one-dimensional (x variable) representation. The fitting procedure renders the values of $\omega_\lambda$ (the so-called albedo, defined in Eq. (3), which quantifies the amount of light scattered by the suspension) and $g_\lambda$ (Eq. (2)) parameters that minimize the differences between model predictions and experimental data of diffuse transmittance and reflectance measurements at the spectrophotometric cell for a set of catalyst concentrations, C, and in the wavelength range of the light source [69]. Such wavelength range is the same where the extinction coefficient is measured. Then, the volumetric scattering and absorption coefficients can be obtained as following:

$$\sigma_\lambda = \beta_\lambda * \omega_\lambda \tag{3}$$

$$\kappa_\lambda = \beta_\lambda - \sigma_\lambda \tag{4}$$

The extinction $\beta_\lambda$, scattering $\sigma_\lambda$ and absorption $\kappa_\lambda$ coefficients, as well as the asymmetry factor g for representative samples of the study are presented in Fig. S3.

#### 2.3.2. Determination of the radiation field in the reactor

Once the optical properties of the catalyst(s) have been obtained, the evaluation of the radiation field inside the photoreactor can be carried out. The DOM tool was used to transform the integro-differential equation 1 into a system of algebraic equations that can be solved numerically. Our reactor configuration requires the use of a cylindrical two-dimensional ($r - z$ variables; the coordinate origin is taken at the center of the upper liquid surface), two-directional
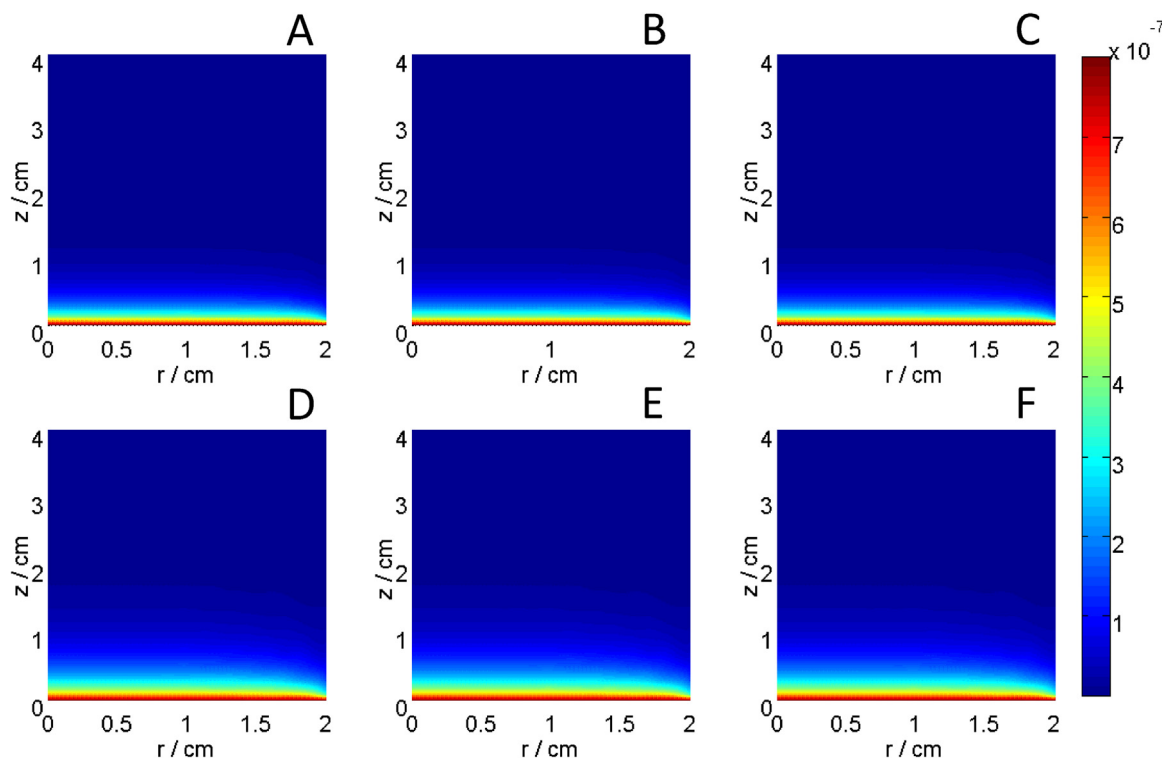
**Fig. 2.** Liquid phase local volumetric rate of photon absorption (Einstein cm$^{-3}$ s$^{-1}$) under UV (A-C) and Visible light (D-E) for representative samples (from right to left Ti/Pt, 0.025NbTi/Pt, 0.075NbTi/Pt).

($\theta - \phi$ variables) model of the photoreactor radiation field (Fig. S2B-C). The net radiation intensity at each $r - z$ point of the reactor is now represented using a discretized spatial mesh having two angular-related coordinates $\mu = \cos(\theta)$ ; $\eta = \cos(\phi)$. Fig. S2C displays $\mu$ ; $\eta$ unitary, basal projection(s) in a quadrant of the space around a $r - z$ point calculated using the so-called S$_{16}$ method [70]. The obtention of the intensity at each point of the reactor requires dividing the space in 4 quadrants as depicted in Fig. S2D, and the measurement of the incident light intensity at the boundary (liquid surface) using actinometry [71]. According to the Duderstadt and Martin recommendation [72], and following the numerical procedure scheme detailed by previous authors [70], the finite difference (DOM) was derived directly from the radiation balance at each mesh cell (Fig. S2D).

Using the DOM approach the central intensity at each spatial cell ($I_m^{i,j}$) can be calculated from the previous ones starting from the appropriate boundary values ($I_m^{i\pm1/2,j}$;$I_m^{i,j\pm1/2}$) as well as one "auxiliary" one coming from the so-called directional mesh ($I_{m-1/2}^{i,j}$) as:

$$I_m^{i,j} = |mu_m|(A_{i+1/2,j} - A_{i-1/2,j})D^{-1}I_m^{i\pm1/2,j}$$

$$+2|eta_m|B_{i,j}D^{-1}I_m^{i,j\pm1/2} + (A_{i+1/2,j} - A_{i-1/2,j})$$

$$\cdot(nu_{m+1/2} + \nu_{m-1/2})D^{-1}W_m^{-1}I_{m-1/2}^{i,j}$$

$$+\frac{\sigma_\lambda}{4\pi}\sum_{n=1}^{M} I_n^{i,j}P_{nm}W_nV_{i,j}D^{-1} \quad (5)$$

Where constants and variables are defined in the Supporting Information file (see section "details of the numerical procedure for $I_{\lambda,\Omega}$ calculation"). Calculation starts from a corner of the spatial mess where the intensity is defined by boundary conditions and follows through the contiguous cells up to the next frontier. Convergence is reached with intensities varying below 1%.

Once the intensities were obtained, the local volumetric rate of photon absorption ($e^{a,v}$) was calculated at each $r - z$ point of the reactor according to:

$$e^{a,v} = \int_\lambda \kappa_\lambda(\underline{x}) \cdot \int_{\Omega=4\pi} I_{\lambda,\Omega}(\underline{x}) d\Omega d\lambda \quad (6)$$

As mentioned, the solving of the radiative transfer equation (RTE) renders $I_{\lambda,\Omega}$ (required in equation 6 and calculated over all spatial directions and lambdas of the light source) in the heterogeneous reactor used to measure photocatalytic properties. This allows the calculation of the $e^a$ parameter at each point of the reactor; using two different $\lambda$ ranges in the integral of equation 6, to take into account the two illumination sources utilized in this work. The $e^a$ parameter is presented in Fig. 2 for representative samples. In this figure a "r-z" section of the reactor is shown (the reactor volume is constructed from this section by the azimuthal symmetry having all orientations equal values of the observable).

### 2.3.3. Determination of quantum efficiency

Quantum efficiency is defined, according to the IUPAC recommendation [57] as the ratio of the number of molecules transformed or produced in the reaction to the number of photons effectively absorbed by the sample (Eq. (7)).

$$\eta_q(\%) = 100 \times \frac{2 \times r\left(\text{mol m}^{-3}\text{s}^{-1}\right)}{\langle e^a \rangle\left(\text{Einstein m}^{-3}\text{s}^{-1}\right)} \quad (7)$$

The measurement of the reaction rate for hydrogen production is detailed in subsection 2.2. The reaction rate is affected by a factor 2 considering the number of charge carriers (2 electrons) assumed to be required to produce one H$_2$ molecule. The equation used the volume average of the local volumetric rate of photon absorption.
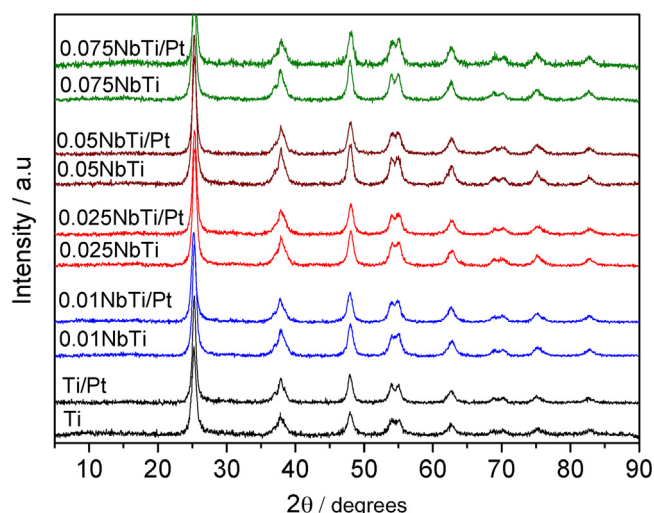
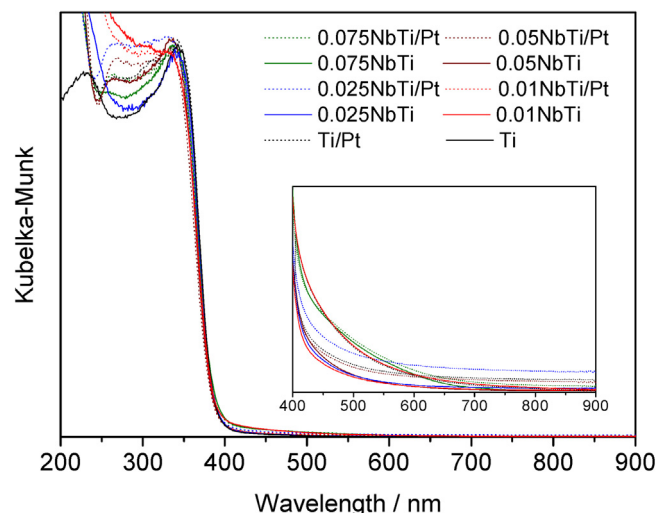**Fig. 3.** XRD diffractograms of the (xNbTi/Pt) samples.



**Fig. 4.** UV–vis spectra of the (xNbTi/Pt) samples.

## 3. Results and discussion

### 3.1. Structural characterization

Fig. 3 collects the XRD patterns of the xNbTi/Pt samples and the corresponding bare xNbTi supports. All peaks in the patterns can be indexed to the anatase polymorph profile (PDF 21–1272; space group I4$_1$/amd). Absence of signals/peaks related to other titania phases or the noble metal can be noticed. The latter is obviously derived from the limited content of platinum at the materials. The XRD anatase peak(s) width displays rather limited differences among all patterns shown in Fig. 3. Primary crystallite sizes of the anatase phase for the samples and bare support(s) references are presented in Table 1. Analysis of these size values indicates that an average value of 12.4 ± 0.6 nm is representative for all samples. In accordance with the limited variation detected in XRD derived physical observables, the BET surface area only shows minor differences (below 10%) among all samples. Table 1 shows a decreasing trend in the surface area values of the samples as the Nb content grows, being this effect of higher significance with respect to platinum deposition. This conclusion is general for morphology parameters as pointed out by the similar behavior of the pore size and volume observables (Table 1).

The UV–vis spectra of the samples, as deduced from the diffuse reflectance spectra of the solids, are collected in Fig. 4. Spectra are dominated by the characteristic band gap of the anatase phase occurring near 400 nm. Considering the anatase samples as indirect gap semiconductors [65], the band gap values summarized in Table 1 can be obtained. Band gap values are constant within experimental error and equal to the Ti reference material as might

be expected from the structural and morphological constancy of the sample properties through the series. Nb doping does not usually modify the band gap of anatase powders but creates a series of localized states typically observed in the Uv-visible spectrum as a tail into the visible region [34,35]. Such effect is detected in our Nb-doped materials (see the inset in Fig. 4) and appears to be of more significance as the Nb content grows and particularly in presence of Pt, indicating a potential relationship of the metal and surface defects. Such point can be of importance to render active photoactive materials upon visible light illumination.

The characterization of the samples was completed with the help of the XPS and TEM techniques. Ti 2p, Nb 3d, and Pt 4f XPS peaks of the samples are depicted in Fig. 5. Corresponding binding energies as well as representative fitting examples are summarized in Table S2 and Fig. S4 at the supporting information section. Constant values of 458.2$_5$ ± 0.05 (Ti2p$_{3/2}$) and 209.3 ± 0.1 (Nd3d$_{5/2}$) eV for all samples of the study are obtained. These values correspond to Ti(IV) and Nb(V) oxidation states [34,73], which are thus dominant (no evidence of reduced states according to fitting results; see Fig. S4 at the supporting information section) in all samples, irrespective of their chemical composition. Nb(V) tends to present a heterogeneous distribution at the anatase nanoparticles, with a (moderate) concentration gradient with maximum at the bulk of the material as suggested by the Nb/Ti XPS ratio (Table S2). Such concentration gradient is not obvious for samples having content below ca. 0.05 mol%. Presence of Nb at the anatase structure was corroborated using Raman spectroscopy. In Fig. S5 of the supporting information we present the Raman spectra of selected samples, which confirm the absence of a significant quantity of surface Nb entities due to the lack of signals at ca. 970–990 cm$^{-1}$, attributable

**Table 1**
Morphological and optical properties of the samples.[a]

| Sample | Size (nm)TiO$_2$ | BET Surface area(m$^2$ g$^{-1}$) | Pore volume(cm$^3$ g$^{-1}$) | Pore size (nm) | Band Gap(eV) |
|---|---|---|---|---|---|
| Ti | 12.5 | 85.2 | 0.134 | 5.72 | 3.18 |
| Ti/Pt | 12.3 | 82.1 | 0.129 | 5.55 | 3.18 |
| 0.01NbTi | 12.1 | 78.0 | 0.121 | 5.19 | 3.18 |
| 0.01NbTi/Pt | 11.8 | 78.1 | 0.122 | 5.15 | 3.16 |
| 0.025NbTi | 12.1 | 81.4 | 0.138 | 5.64 | 3.14 |
| 0.025NbTi/Pt | 11.9 | 80.5 | 0.131 | 5.62 | 3.15 |
| 0.05NbTi | 13.0 | 76.8 | 0.129 | 4.58 | 3.16 |
| 0.05NbTi/Pt | 12.8 | 76.1 | 0.121 | 4.53 | 3.16 |
| 0.075NbTi | 12.8 | 73.4 | 0.108 | 5.11 | 3.16 |
| 0.075NbTi/Pt | 12.4 | 72.5 | 0.105 | 5.13 | 3.15 |

[a] Average Standard error: Size 8%; BET area 5%; pore size/volume 5.5%; band gap; 1.5%.
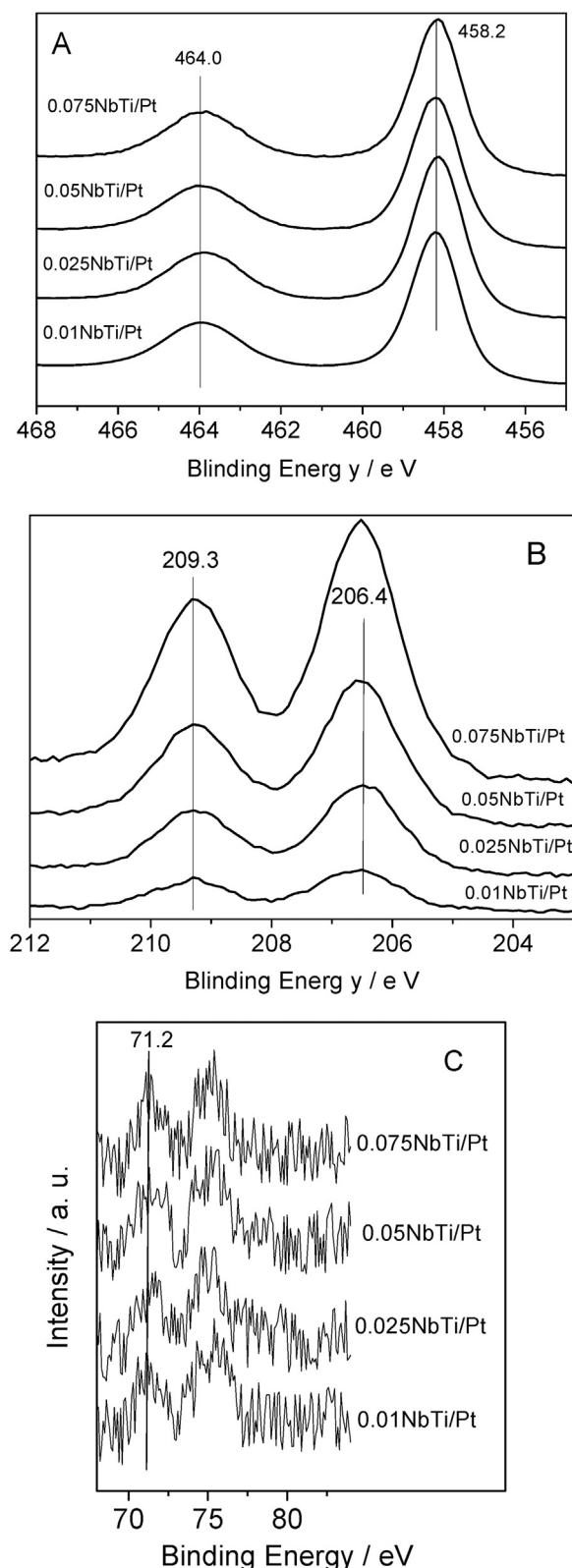
**Fig. 5.** XPS data of the (xNbTi/Pt) samples: (A) Ti 2p; (B) Nb 3d; and (C) Pt 4f peaks.

to Nb=O bonds [74]. The Nb heterogeneous location within the anatase particle (the only phase detected by XRD) is therefore supported by all experimental measurements and appears in line with previous results where the physico-chemical effects of the Nb substitution are discussed [33,35,75]. Nb tends to favor homocation (Nb—O—Nb) vs heterocation (Nb-O-Ti) bonds where sited at the

bulk of anatase, leading to complex charge neutrality defects, likely responsible of the absorption detected in the visible region [33].

The limited noble metal loading and the high dispersion of the Pt metal (modulating metallic type states by quantum confinement) make difficult to obtain clean Pt 4f XPS signals. The Pt 4f core level signal is overlapping with the Ti 3 s plasmon loss signal, a fact that increases the complexity of the analysis [73]. Note also that alternative Pt core level peaks such as Pt 4d (recorded for our samples; not shown) or others are not useful due to the strongly limited intensity displayed in the case of our samples. Pt 4f peaks for the samples are presented in panel C of Fig. 5. Although the signal to noise ratio (roughly 3) precludes a good fitting analysis or even a detailed shape analysis of the XPS spectra, the Pt 4f contribution displays a maximum at ca. 71.2 eV for all samples. As metallic Pt has a 4f characteristic binding energy at 70.8 eV [73,76], a metallic state would be dominant for all samples. This is in line with previous reports studying platinum deposition on titania where an inert atmosphere was utilized [77], as is here the case.

The analysis of the metallic and oxidic phases of the samples is completed with the help of microscopy. As illustrated in Fig. 6, the metal particles are observed, with rounded shape morphology, dispersed onto anatase entities having characteristic, irregular borders as previously observed for microemulsion prepared anatase powders [78]. We used XEDS to analyze the Nb distribution in the samples. Illustrative results are summarized in Fig. S6 of the supporting information section. The plots at Fig. S6 make obvious that the heterogeneous distribution of the doping cation in the oxide phase grows with the Nb content. The average Nb/Ti ratios obtained, 0.023, 0.050, and 0.081 for, respectively, 0.025NbTi/Pt, 0.05NbTi/Pt, and 0.075NbTi/Pt samples, fit reasonably well with the theoretical values (0.027, 0.054, and 0.081) expected from the initially used reagent amounts. Comparison of these values with the XPS ones again reinforces the idea of a Nb (moderate) content gradient within the anatase particles.

Focusing now in the noble metal particle size distribution, the analysis of TEM images provides the results presented in Fig. 7. Noble metal particles were identified using XEDS and magnified TEM images (see Fig. S6 at the supporting information section). Average primary particle sizes between 1.2 and 1.5 nm are obtained from all xNbTi/Pt samples. The rather small, noble metal average particle size seems in line with previous reports [28,54,56], although as previously mentioned, a fine control of the noble metal particle size is here favored with the use of an inert atmosphere in the preparation step. In Fig. 7 we can also observe relatively narrow Pt primary particle size distributions (variance 0.073, 0.175, 0.299, and 0.093 for, respectively, 0.025NbTi/Pt, 0.05NbTi/Pt, 0.075NbTi/Pt, and Ti/Pt samples). The noble metal distributions of Fig. 7 display a widening with the growth of the average primary particle size and the Nb content. Differences in the noble metal are however relatively modest; a simple calculation of the available surface area assuming spherical FCC particles (as suggested by TEM) provides a dispersion value of $0.84 \pm 0.04$ for all samples.

### 3.2. Photocatalytic properties: measuring and interpreting quantum efficiency

The reaction rates for hydrogen production obtained in the liquid phase experiments using a 3:7 $CH_3OH:H_2O$ ratio are presented in panel A of Fig. 8. Both UV and visible illumination sources were tested in our samples. Note that, as mentioned, the samples present rather limited differences in the noble metal properties and particularly in primary particle size. Nb doping of anatase phase seems to control the chemical response of the samples and to trigger a beneficial effect as compared with the corresponding parent anatase sample, at least for Nb loadings below 7.5 mol%. A positive effect of Nb in photocatalytic elimination of contaminants
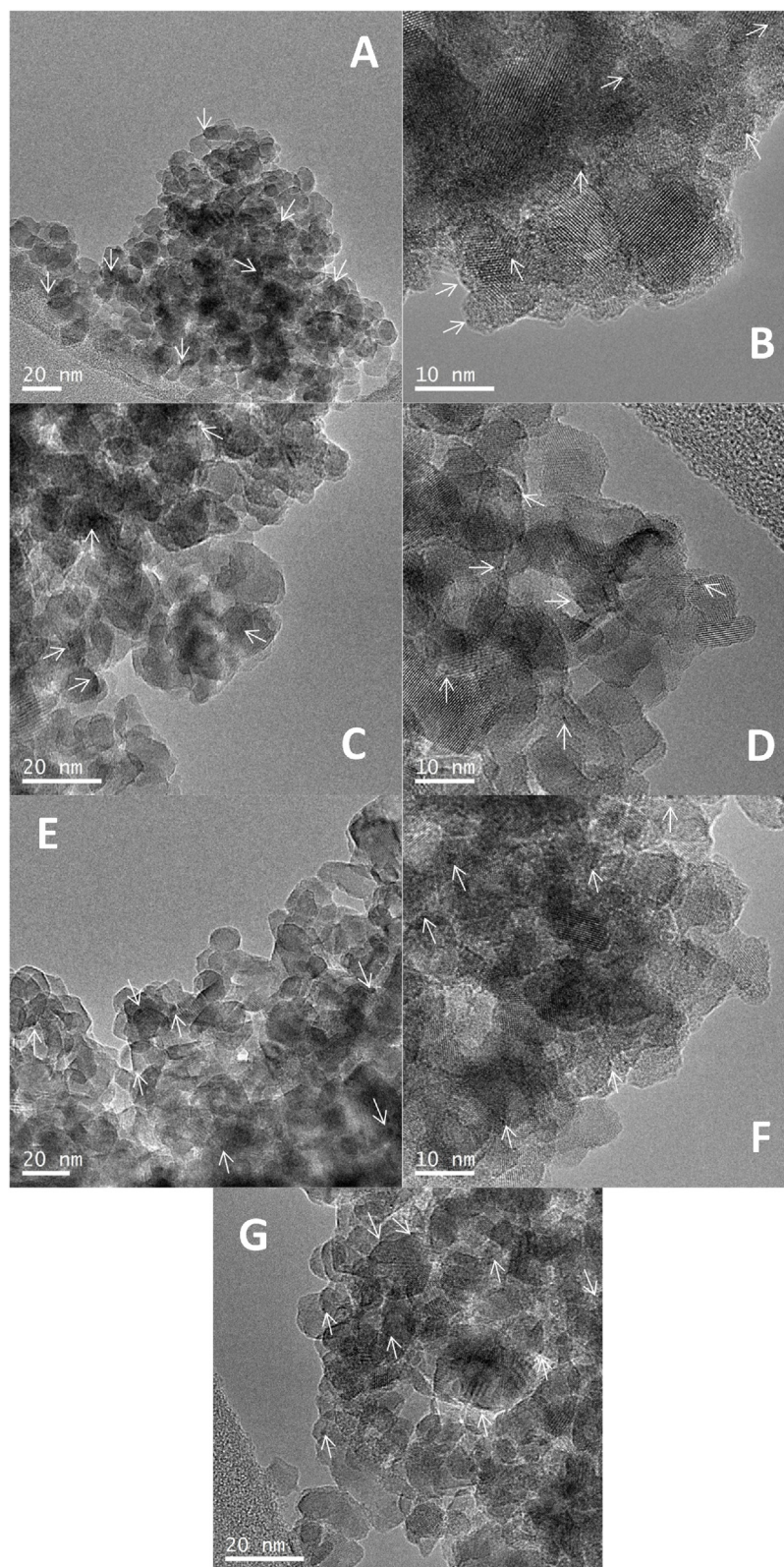
**Fig. 6.** TEM images of (A,B) 0.025NbTi/Pt, (C,D) 0.05NbTi/Pt, (E,F) 0.075NbTi/Pt and G (Ti/Pt).

[31–39] or promoting water oxidation [31] has been previously reported, particularly as a function of the Nb content of the material and the light wavelength, but its use to promote hydrogen production is less studied (in fact we are not aware of any previous results). In the present work, the $H_2$ production rate per gram of catalyst displays a maximum for sample 0.025NbTi/Pt sample irrespective of the excitation wavelength. A relatively similar (near optimum) performance is achieved nonetheless with the 0.05NbTi/Pt sample, particularly under visible illumination. Doping with Nb usually triggers a balance between the positive and
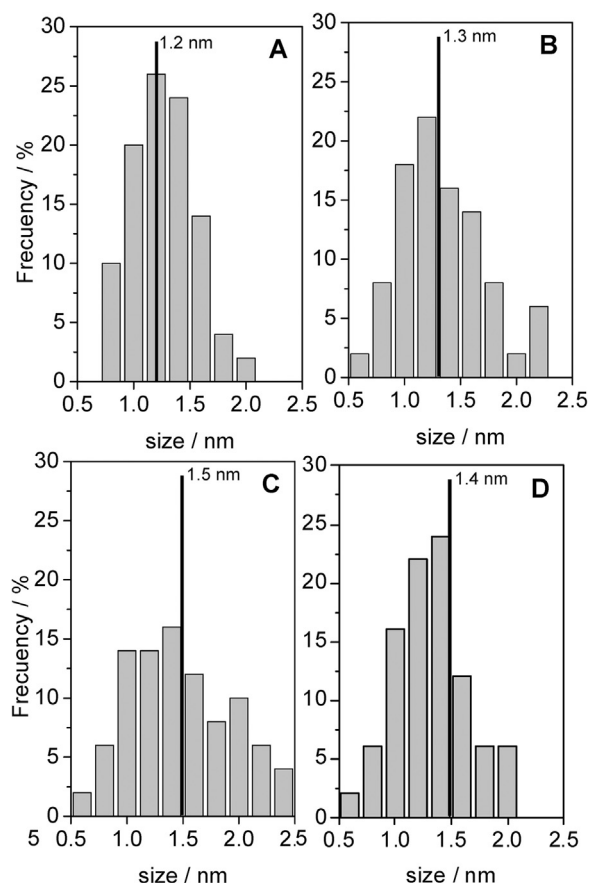
**Fig. 7.** Pt particle size distributions (from TEM data) of (A) 0.025NbTi/Pt, (B) 0.05NbTi/Pt, (C) 0.075NbTi/Pt and (D) Ti/Pt.

negative effects in photoactivity, with modification of the optical and/or surface properties in a favorable way for activity but with concomitant alteration of charge recombination, producing a negative effect in the last process (e.g. increasing recombination) as the doping content grows [2,4].

As mentioned, a beneficial effect is observed for hydrogen photo-production in Fig. 8 with respect to the bare titania support for all materials with Nb contents below 0.075 mol%. This enhancement of the activity observed in panel A of Fig. 8 seems larger under visible than UV illumination conditions. The trend observed in the reaction rate results and, particularly, the ratio between visible and UV reaction rates presented in Fig. 8 (panel B) provide evidence that the increase of Nb content favors the performance upon visible light in relative terms with respect to the UV case. A beneficial effect related to the noble metal influence in activity under visible illumination as a result of the interaction with Nb-induced (surface) titania electronic states can be invoked and was supported by the UV–vis results previously described [2–4]. So, although including Nb leads to maximum activity for the 0.025NbTi/Pt sample irrespective of the illumination wavelength, the relative performance under visible light with respect to UV increases continuously with the Nb content of the materials. This would indicate differences between the two illumination conditions which will be analyzed using the efficiency parameter.

The calculation of the efficiency parameter carried out using numerical methods is presented in Fig. 9. A similar trend in the reaction rate is observed for both illumination conditions, with a maximum corresponding to the 0.025NbTi/Pt samples. Calculation of the quantum efficiency points out, in any case, that noble metal promoted titania samples present maximum values near 5% for
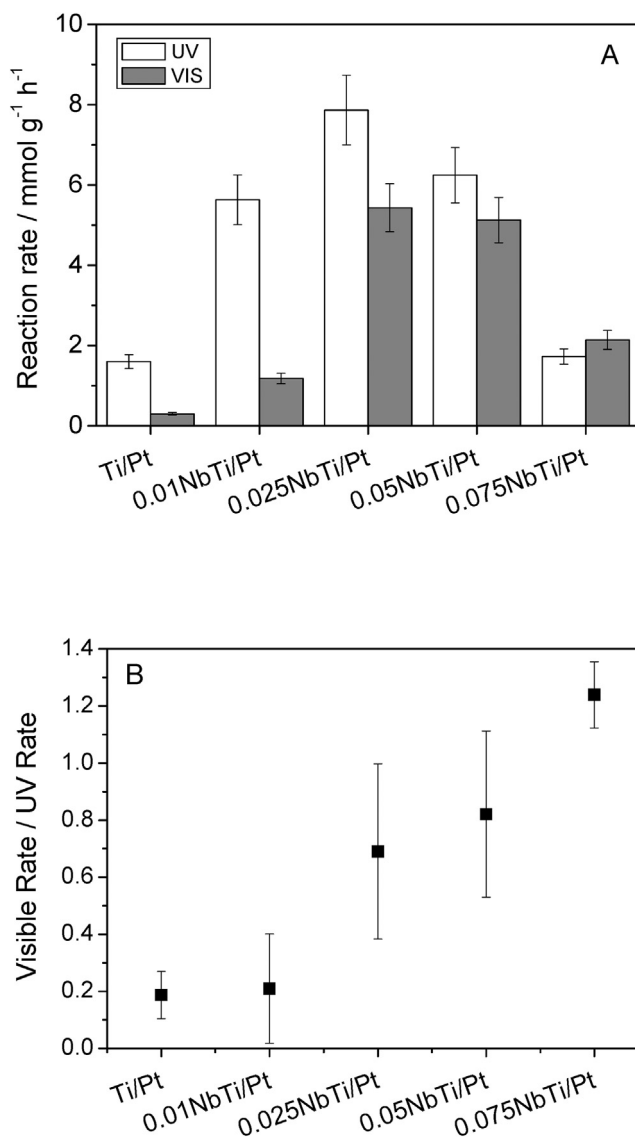


**Fig. 8.** $H_2$ photoproduction rate for the (xNbTi/Pt) samples and Ti/Pt reference using a 3:7 $CH_3OH:H_2O$ reaction media/mixture. (A) rate; (B) ratio between UV and visible values.

UV and 2.5% for visible light (Fig. 9). Comparison with literature is relatively difficult. Metal-promoted titania catalysts containing Pt [16,19], Cu [19,20] or Ni [79] which have been previously published in the literature reported UV photonic or apparent rather than (the so called "true") quantum efficiency values ranging typically from ca. 2 to 10%. A lower number of reports can be found concerning the quantum efficiency for hydrogen production. To our knowledge, the efficiency was reported for Pt-promoted titania-based systems under UV excitation (more exactly in ranges from ca. 300 nm to below 410–420 nm) in tree cases. De Lasa and coworkers analyzed several systems and found values of ca. 4.6% and 5.7% for 1 wt.% Pt (the catalyst with noble metal properties more close to ours among the ones tested) at natural pH for, respectively, Degussa P25 and mesostructured (home-made) titania based materials [80,81]. A recent paper also showed a ca. 5.5% for the same loading used here but for a P25 supported sample [62]. Under sunlight-type excitation, we only found a carbon nitride based material displaying quantum efficiencies below 2% [82]. So, the summary of literature reports just presented indicates that the systems here presented are competitive with literature reports.
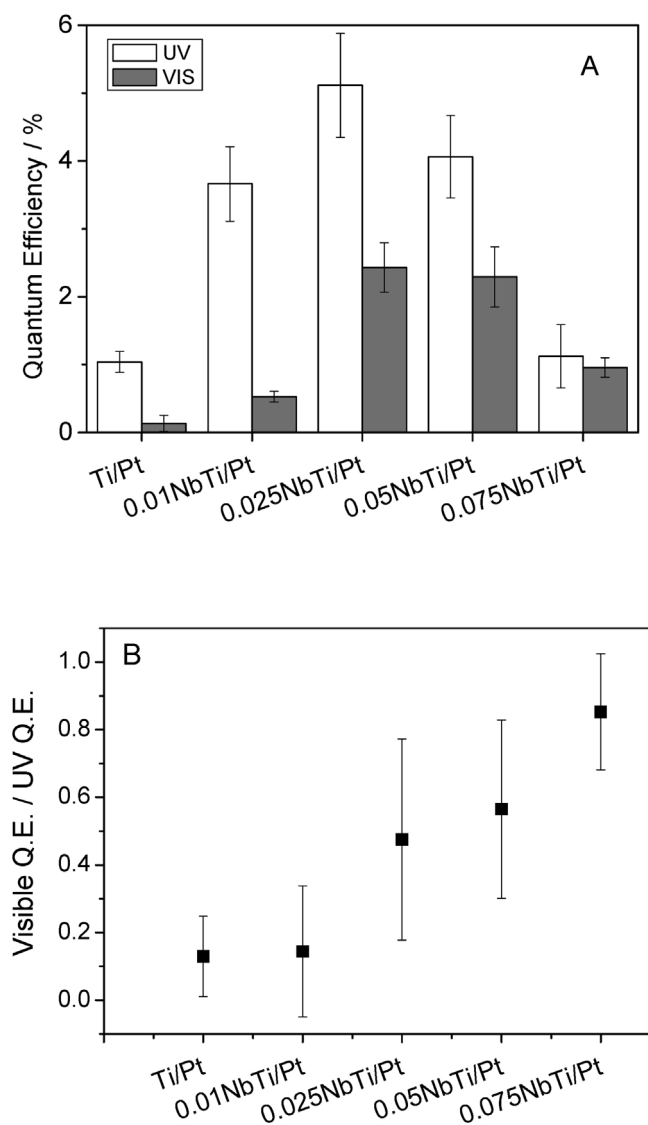
**Fig. 9.** $H_2$ photoproduction quantum efficiency for the samples (xNbTi/Pt) and Ti/Pt reference using a 3:7 $CH_3OH:H_2O$ reaction media/mixture. (A) rate; (B) ratio between UV and visible values.

To complete the catalytic characterization, we further analyze the performance of the 0.025NbTi/Pt sample under different reaction conditions differing in the methanol to water ratio, illumination intensity, and photocatalyst concentration. Contour plots illustrating the quantum efficiency results (details of the Box-Behnken design [83] utilized are presented at the supporting information section; "Photocatalytic properties: design of the experiments") are shown in Fig. 10. Again, UV and visible illuminations were studied, presenting similar trends. The catalytic effect of the $CH_3OH:H_2O$ ratio has been particularly analyzed in the literature [84,85]. In general, optimum activity is obtained in those works with ratios from ca. 2:8 to 5:5. In line with the mentioned literature results, here we observed an optimum for the quantum efficiency at ca. 4:6 ratio, the latter being nearly the same for the UV and visible spectrum regions. Discussing light intensity (which was adjusted using neutral filters), we observed a relatively strong effect of intensity. Representing such dependence in an approximate way with a power of the intensity we observed an average value of the exponent of ca. 0.5. Such value is representative of relatively intense illumination conditions [86]. Finally the sample weight shows optimum values near ca. 0.4 mg mL$^{-1}$ upon both illu-

mination conditions. Using the factorial design study, we obtained a quantum efficiency maximum value of ca. 6.5% and 3.0% under, respectively, UV and visible light illumination. These values were maintained (within a 4.5% error) in a stability test for 12 h of time on stream.

The ratio between visible and UV light quantum efficiencies along our sample series is presented in panel B of Fig. 9. The factorial design study presented in Fig. 10 for the 0.025NbTi/Pt sample indicates that the conclusions that can be extracted from such (visible vs. UV) comparison essentially hold for all experimental conditions and not only for those presented in Fig. 9. As previously occurring with the ratio of the corresponding reaction rates, we observed an increase of the quantum efficiency ratio as the Nb content of the titania phase grows. So, although there can be some differences in optical absorption by the materials as a function of the Nb content (Fig. S4), they do not alter the trend presented by the reaction rate, which is essentially maintained in the efficiency parameter and thus in an observable normalized per incident, adsorbed photon. Thus, although the optimum found at a 2.5 mol% Nb would likely indicate that recombination losses are important to understand the catalytic behavior of such sample, the Nb induced electronic states responsible for visible light absorption are still active and generate photon-induced chemistry for loadings above that maximum. The increasing improvement in that ratio observed with the Nb content (Fig. 9) is of importance for achieving maximum profit of sunlight. For a AM1.5 solar spectrum standard, the measurement of the efficiency presented in Fig. 9 allows to estimate for sunlight (a similar derivation as above based on reaction rates or apparent quantum efficiencies values is not possible) a maximum quantum efficiency of ca. 3.5%. As mentioned, this is a significantly larger value than those obtained by Pt-promoted carbon nitride materials under sunlight illumination [82].

We explore the influence of the charge recombination issue with the help of photoluminescence studies of the materials under UV (320 nm) and visible (450 nm) excitation. Photoluminescence experiments are presented in Fig. 11. Excitation under UV (320 nm) shows the typical photoluminescence spectra of the reference sample, the anatase bare oxide. Such spectrum is composed in fact by two types of transitions corresponding to the annihilation of conduction band free electrons with trapped holes and valence band free holes with trapped electrons [87,88]. It therefore provides direct information about the recombination processes occurring in the solids after illumination. The transitions are usually called green and red due to the average energy of the transition, ca. 450 nm from the green and above 550 nm for the red. Our samples display rather similar spectra with broad peaks at ca. 425, 480 and 550 nm (Fig. 11). Samples display only marginal differences with the titania-based reference and there is not a consistent trend (with respect to the reference) as a function of the Nb content. The quantum efficiency maximum at 0.025NbTi/Pt points out the fact that Nb influence on recombination is not so critical and that other effects may be responsible of the overall trend presented by the efficiency parameter. The photoluminescence spectra under visible (450 nm) illumination show the typical relatively weak signals associated to defect state(s) de-excitation over a decay curve corresponding to the excitation line [87–89]. Again we did not observe a neat relationship between the effect of Nb on charge recombination and activity, as the optimum, Nb-containing samples display larger intensity in all de-excitation peaks than the bare titania reference. This points out that upon UV and visible light excitation, the effect of Nb on charge recombination would certainly alter the behavior of the bare titania reference but is not determining the quantum efficiency behavior through the sample series shown in Fig. 9.

Note that according to the characterization results, the behavior of the efficiency would not be primarily related to a shadowing effect by accumulation of Nb species at the (active) anatase surface
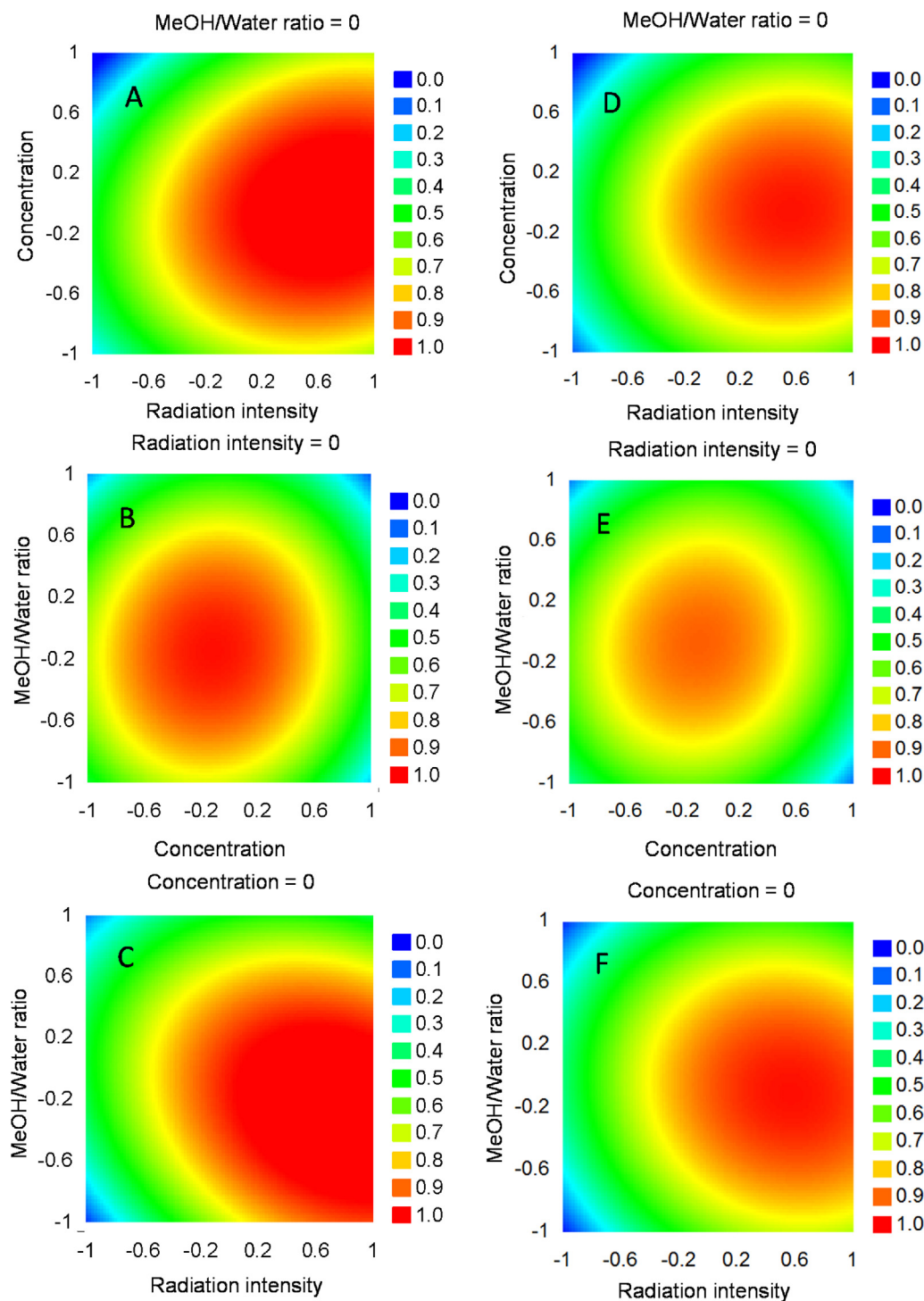
**Fig. 10.** Countour plots of the 0.025NbTi/Pt liquid phase quantum efficiency as a function of (A,D) radiation intensity and catalyst concentration, (B,E) catalyst concentration and $CH_3OH/H_2O$ molar ratio, and (C,F) radiation intensity and $CH_3OH/H_2O$ molar ratio. (A,B,C) UV illumination; (D,E,F) Visible illumination. The axes values correspond to the relative levels according to the design of experiment presented in supporting information (Fig. S5).

as such cation is at substitutional positions of the structure and presents some tendency to be at the bulk. So, considering such fact and the (relatively limited) Nb atomic content of the samples, we can anticipate a modest effect of a potential shadowing effect in the catalytic performance. Rather than this, we suggest that the presence of Nb at the surface or near surface regions may alter the number or properties of the radical species responsible for the attack to the sacrificial molecule (e.g. holes) or the production of hydrogen (electrons).
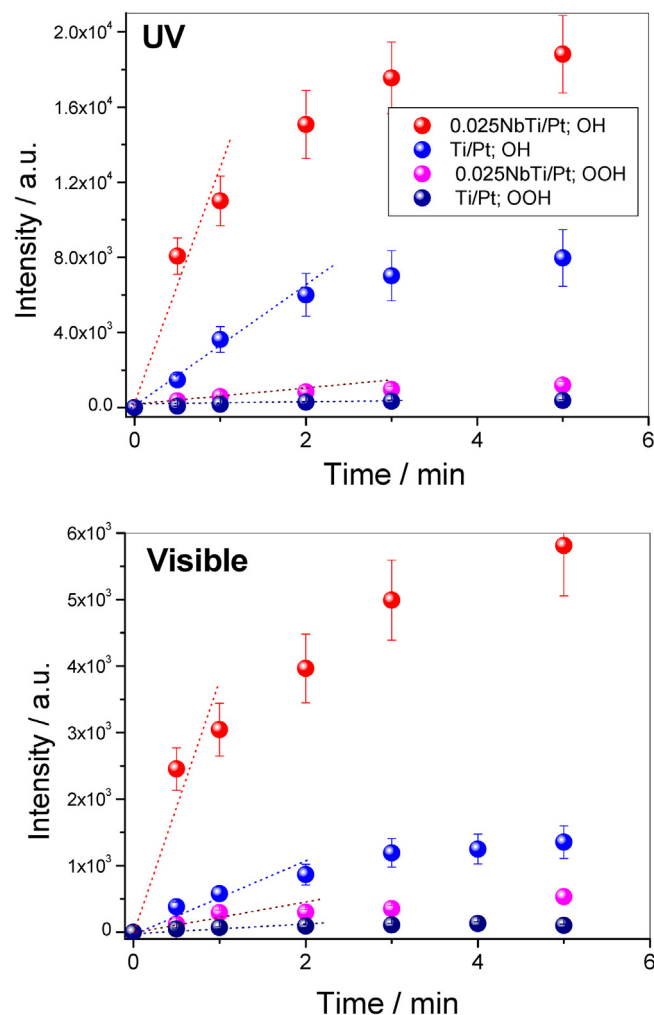
To prove that this is can be the case, we explore the formation of such radicals at the surface using electron paramagnetic reso-nance. UV and visible irradiation (using the light sources as in the photochemical reactor) of DMPO-containing sample water suspen-sions gives rise to a signal presented in Fig. S8 of the supporting information section. Such signal displays a 1:2:2:1 intensity pat-tern (Fig. S8). Its EPR parameters (g = 2.0056, $a_N$ = 14.9 G, $a_H$ = 14.9 G) are characteristic of DMPO-OH adducts generated by the reaction of the probe molecule and hole-derived OH radicals [90,91]. The
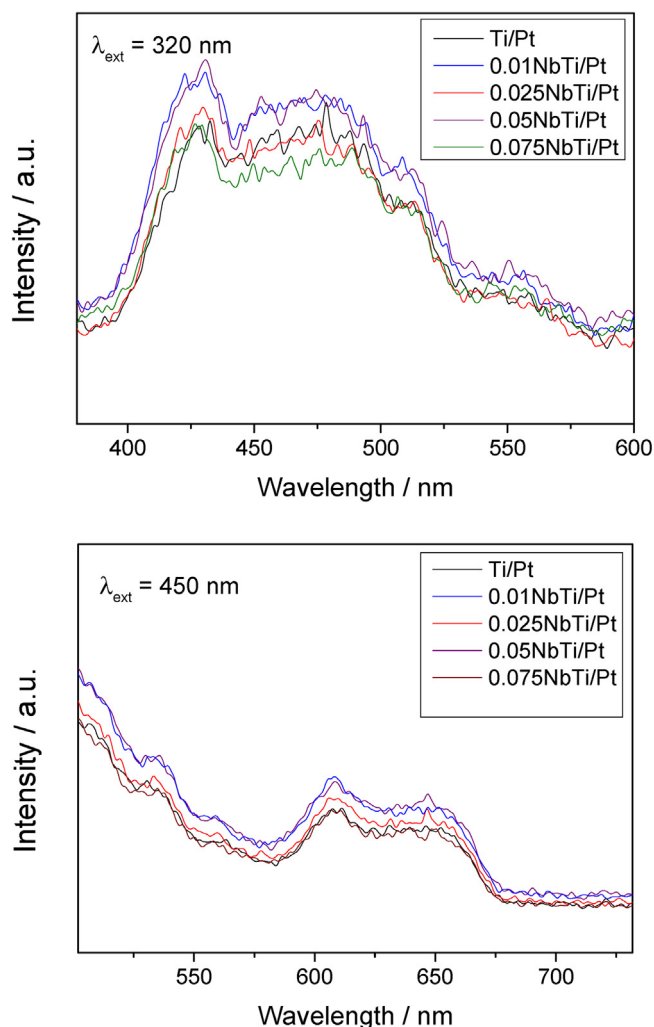
**Fig. 11.** Photoluminescence spectra of samples (xNbTi/Pt) and Ti/Pt reference under (upper panel) 320 nm and (lower panel) 450 nm excitation.



**Fig. 12.** Evolution of the radical species signal intensity for the experiments presented in Fig. S8 as a function of irradiation time upon UV and visible illumination conditions. Lines correspond to the initial slope for radical formation.

accumulation of DMPO-OH adducts grows continuously in all cases but such radicals have a limited stability, so that a maximum concentration as a function of irradiation time is always detected (if enough time is scanned). The latter is an effect of multiple additions, within consecutive reactions, of OH radicals to DMPO molecules to yield diamagnetic species [90–92]. Similarly, The experiments carried out using methanol as solvent (see Fig. S8 at the supporting information section) show the formation of the DMPO-OOH adduct created by interaction of the probe molecule and the superoxide radical ($O_2^{-\bullet}$) formed upon capture of an electron by the $O_2$ molecules present, which is subsequently protonated. This species has as EPR parameters, $g = 2.0056$, $a_N = 13.1$ G, $a_H = 12.1$ G [93,94]. The OH radical adduct is not observed here, due surely to its efficient capture by the methanol molecules present in high concentration, allowing to observe the OOH adduct which is formed in much lower concentration. This radical species serves here as a fingerprint to get comparative information on the number of electrons that reach the surface of the anatase at the materials in this experiment, although one may assume that most of the electrons will be captured by the metal particles.

The intensity of these two electron paramagnetic resonance (EPR) signals is plotted in Fig. 12 as a function of the irradiation time. As mentioned, to compare catalysts we use the initial rate of formation. The values of this observable are collected in Table 2. A first comment is related to the fact that the formation of hydroxyl-

**Table 2**
Values of initial rates of radical formation ($r_{OH\bullet}$ and $r_{OOH\bullet}$) as measured with EPR.[a]

| $r\left[\dfrac{\text{Number of spins}}{\text{min}}\right]$ | OH•/UV | OH•/Visible | OOH•/UV | OOH•/Visible |
|---|---|---|---|---|
| Ti/Pt | 3273 | 548 | 121 | 65 |
| 0.025NbTi/Pt | 12825 | 3820 | 488 | 224 |

[a] Standard error: 18.5%.

type radicals in absence of methanol is always favored if compared with the electron one. The capture of electrons by the metal would lead to EPR silent species (delocalized electrons in the metal, $H_2$ molecules and/or $O_2H_2$ depending on the experimental conditions) not accounted for in these experiments. According to the TEM (noble metal size and exposed surface) and photoluminescence (recombination) experiments, the differential (electron trapping) effect of Pt in going from one sample to other is expected to be relatively minor, independently of the excitation wavelength. Thus, with the electron capture experiment we only attempt to measure (in a first approximation) differences between the 0.025NbTi/Pt and the Ti/Pt samples rather than discussing the charge handling of electron related species in each sample.

From the EPR experiments, we note that the hydroxyl radical number follows qualitatively the trends of the activity. The 0.025NbTi/Pt sample shows higher values than the Ti/Pt sample but also presents a higher visible to UV ratio for the generation rate of

hydroxyl-type radicals. Such results strongly suggest that the separation of charge and specific surface properties of catalysts obtained in presence of Nb at the anatase component cooperatively work in order to enhance the number of charge carrier species reaching the catalyst surface and able to transform the sacrificial molecule, rendering hydrogen in the process. In this context, we note that such surface modification by Nb does not modify significantly the chemical product of the alcohol transformation as formic acid was essentially the only product detected with liquid chromatography (selectivity >97%). So, the effect of Nb is focus on opening new surface sites that otherwise transform the sacrificial molecule in an essentially similar way than the Nb-free anatase material.

## 4. Conclusions

In this work we studied the hydrogen photo-production in platinum supported on Nb-doped anatase under UV and visible light illumination conditions. The photocatalyst samples were characterized with a multitechnique approach to provide evidence that the Pt and the anatase-titania phases display rather similar physicochemical characteristics among the samples of the series. In fact, the noble metal displays a rather limited primary particle size between 1.0 and 1.5 nm and has a dominant zero-valent state for all samples tested. Nb is shown to be located at the anatase structure for all samples but with some tendency to be at the bulk of the nanoparticles.

The photocatalytic results were analyzed in terms of the quantum efficiency, determined numerically using a model of the reactor system. The presence of Nb of the materials renders photoactive materials under both UV and visible illumination. Nb-containing $TiO_2$ catalysts overperform the corresponding bare $TiO_2$ reference, rendering a maximum for a loading of 2.5 mol% of Nb. This maximum displays a quantum efficiency of ca. 6.5 and 3.0% for, respectively, UV and visible illumination conditions. The combination of photoluminescence spectroscopy and electron paramagnetic resonance was used to elucidate the physicochemical roots of the behavior of the samples. From such study we propose that Nb opens new active sites at the anatase surface which chemically transform the sacrificial molecule in a similar way than the bare anatase surface. Thus, the enhanced efficiency is not directly related to the effect of Nb on charge recombination but would depend critically on the modification of the surface to promote the transformation of the sacrificial molecule.

## Acknowledgements

## Appendix A. Supplementary data

Supplementary data associated with this article can be found, in the online version, at http://dx.doi.org/10.1016/j.apcatb.2017.05.022.

## References

[1] N. Vecirolu, F. Barbir, Int. J. Hydrog Energy 17 (1992) 391–404.
[2] X. Chen, S.S. Chen, L. Guo, S.S. Mao, Chem. Rev. 110 (2010) 6503–6570.
[3] K. Maeda, K. Domen, J. Phys. Chem. Lett. 1 (2010) 2655–2661.
[4] A. Kubacka, M. Fernández-García, G. Colón, Chem. Rev. 112 (2012) 1555–1614.
[5] K. Villa, X. Domenech, S. Malato, M.I. Maldonado, J. Peral, Int. J. Hydrog. Energy 38 (2013) 12718–12724.
[6] Y. Ma, X. Wang, Y. Jia, X. Chen, H. Han, C. Li, Chem. Rev. 114 (2014) 9987–10043.
[7] X. Li, J. Yu, J. Low, Y. Fang, J. Xiao, X. Chen, J. Mater. Chem. A 3 (2015) 2485–2534.
[8] T. Kawan, T. Sakata, Nature 286 (1980) 474–476.
[9] A. Galinska, J. Walendziewski, Energ. Fuels 11 (2005) 1143–1147.
[10] Y.X. Li, Y.Z. Me, S.Q. Peng, G.X. Lu, S.B. Li, Chemosphere 63 (2006) 1312–1318.
[11] A. Pastora, D.I. Kondarides, X.E. Verykios, Catal. Today 124 (2007) 94–102.
[12] X. Fu, J. Long, X. Wang, D.C.Y. Leung, Z. Ding, L. Wu, Z. Zhang, Z. Li, X. Fu, Int. J. Hydr. Energy 33 (2008) 6484–6491.
[13] W. Sun, S. Zhang, Z. Liu, W. Wang, Z. Mao, Int. J. Hydr. Energy 33 (2008) 1112–1117.
[14] M. Bouker, Catal. Lett. 142 (2012) 923–929.
[15] Y. Ma, Q. Xu, X. Zong, D. Wang, G. Wu, X. Wang, C. Li, Energy Environ. Sci. 5 (2012) 6345–6351.
[16] E. Pulido Melián, J.A. Ortega Méndez, C. Rodríguez López, M. Nereida Suárez, J.M. Doña Rodríguez, J.A. Navío, D. Fernández Hevia, Int. J. Hydr. Energy 38 (2013) 11737–11748.
[17] D. Slament, V. Tristanidi, M. Ibadurrbhran, Enery Res. 37 (2013) 1372–1381.
[18] G.N. Nomikos, P. Panagiotopoulous, D.I. Kondarides, X.E. Verykios, Appl. Catal. B 146 (2014) 249–257.
[19] A. Kubacka, M.J. Muñoz-Batista, M. Fernández-García, S. Obregón, G. Colón, Appl. Catal. B 163 (2015) 214–222.
[20] S. Obregón, M.J. Muñoz-Batista, M. Fernández-García, A. Kubacka, G. Colón, Appl. Catal. B 179 (2015) 468–478.
[21] Y.-J. Yuan, J.-R. Tu, Z.-J. Ye, Z.-T. Yu, Z.-G. Zou, Appl. Catal. B 188 (2016) 13–22.
[22] Z. Chen, X. Jian, C. Zhu, C. Shi, Appl. Catal. B 199 (2016) 241–251.
[23] Q. Hu, J. Huan, G. Li, J. Chen, Z. Zhang, Z. Deng, Y. Jiang, W. Guo, Y. Cao, Appl. Surf. Sci. 369 (2016) 201–206.
[24] M. Zhang, R. Sun, Y. Li, Q. Shi, L. Xie, J. Chen, X. Xu, H. Shi, W. Zhao, J. Phys. Chem. C 120 (2016) 10746–10756.
[25] J.G. Highfield, M.H. Chen, P.T. Ngyen, Z. Chen, Energy Environ. Sci. 2 (2009) 991–1002.
[26] G.L. Chiarello, M.H. Aguirre, E. Selli, J. Catal. 273 (2010) 182–190.
[27] T.A. Kandiel, I. Ivanova, D.W. Bahnemann, Energy Environ. Sci. 7 (2014) 1420–1426.
[28] A. Naldom, M.D. Ángelo, M. Altomare, M. Morelli, R. Scott, F. Morazzoni, E. Selli, V. Del Santo, Appl. Catal. B 130-131 (2013) 239–248.
[29] G. Colón, Appl. Catal. A 518 (2016) 48–59.
[30] L.R. Sheppard, T. Bak, J. Nowotny, J. Phys. Chem. B 110 (2006) 22447–22454.
[31] W. Li, T. Bak, A. Atanacio, J. Nowotny, Appl. Catal. B 198 (2016) 243–253.
[32] A. Mattson, M. Leideburg, K. Larsson, G. Westin, L. Osterlund, J. Phys. Chem. B 110 (2006) 1210.
[33] A. Kubacka, M. Fernández-García, G. Colón, J. Catal. 254 (2008) 272–284.
[34] A. Kubacka, G. Colón, M. Fernández-García, Catal. Today 143 (2009) 286–292.
[35] J. Wang, X. Zhang, C. Wang, B. Xia, Y. Liou, Solid State Sci. 14 (2012) 139–144.
[36] H. Zand, M.H. Ang, M.O. Tade, Int. J. Photoener. (2012) 548158.
[37] L. Kong, C. Wang, H. Zheng, X. Zhang, Y. Liu, J. Phys. Chem. C 119 (2015) 16623–16632.
[38] Y. Kou, J. Yang, B. Lee, S. Fu, Mater. Res. Bull 63 (2015) 105–111.
[39] S.G. Ghugal, S.S. Umare, R. Sasikala, Mater. Res. Bull. 61 (2015) 298–305.
[40] W.-J. Ong, L.-L. Tang, S.-P. Chai, S.-T. Yong, A.R. Mohamed, ChemSusChem 7 (2014) 690–719.
[41] D. Wang, T. Hisatomi, T. Takata, C. Pan, M. Katayama, J. Kubota, K. Domen, Angew. Chem. Int. Ed. 52 (2013) 11252–11256.
[42] S. Trasatti, J. Electroanal. Chem. 39 (1972) 163–171.
[43] Y. Li, G. Lu, S. Li, Appl. Catal. A 214 (2001) 179–185.
[44] S. Yin, T. Sato, J. Photochem. Photobiol. A 169 (2005) 89–94.
[45] W.T. Teoh, L. Madler, R. Amal, J. Catal. 251 (2007) 271–280.
[46] C.-H. Lin, J.-H. Chao, C.-H. Liu, J.-C. Chang, F.-C. Wang, Langmuir 24 (2008) 9907–9915.
[47] J.S. Jang, S.H. Choi, H.G. Kim, J.S. Lee, J. Phys. Chem. C 112 (2008) 17200–17205.
[48] M. Alam Kahn, M. Shaherr Akhtar, S.I. Woo, O.-B. Yang, Catal. Comm. 10 (2008) 1–5.
[49] H. Wang, Z. Wu, Y. Liu, Y. Wang, Chemosphere 74 (2009) 773–778.
[50] T. Sreethawong, C. Junbua, S. Chavadej, J. Power Sourc. 190 (2009) 513–524.
[51] Y. Jiaguo, Q. Lifang, M. Jaroniec, J. Phys. Chem. B 114 (2010) 13118–13125.
[52] J. Liu, G. Liu, M. Li, L. Jiang, Y. Song, Energy Environ. Sci. 3 (2010) 1503–1506.
[53] S. Obregón, G. Colón, Appl. Catal. B 144 (2014) 775–782.
[54] Z.H.N. Al-Azri, W.-T. Chen, A. Chan, T. Ina, H. Idriss, G.N. Watterhose, J. Catal. 329 (2015) 355–367.
[55] Y.H. Li, C. Peng, S. Yuang, H.F. Wang, H.G. Yang, J. Catal. 330 (2015) 120–128.
[56] Z. Jiang, Z.Y. Zhang, W. Shangguan, M.A. Isaacs, L.J. Durndell, C.M.A. Parlett, A.F. Lee, Catal. Sci. Technol. 6 (2016) 81–88.
[57] S.E. Braslavsky, A.M. Braun, A.E. Cassano, A.V. Emeline, M.I. Litter, L. Palmisano, V.N. Parmon, N. Serpone, Pure Appl. Chem. 83 (2011) 931–1014.
[58] R.L. Romero, O.M. Alfano, A.E. Cassano, Ind. Eng. Chem. Res. 36 (1997) 3095–3109.
[59] H.I. Lasa, B. Serrano, M. Salaices, Photocatalytic Reaction Engineering, Springer, 2005, 2017, pp. 63–96 (Chpt 4).
[60] J. Marugán, R. van Grieken, A.E. Cassano, O.M. Alfano, Appl. Catal. B: Environ. 85 (2008) 48–60.
[61] M. Salaicesa, B. Serranoa, H.I. de Lasa, Chem. Eng. Sci. 59 (2004) 3–15.
[62] O. Fontelles-Carceller, M.J. Muñoz-Batista, E. Rodríguez-Castellón, J.C. Conesa, M. Fernández-García, A. Kubacka, J. Catal. 347 (2017) 157–169.
[63] G.K. Willianson, W.H. May, Acta Metall. 1 (1953) 22–29.
[64] P. Kubelka, J. Opt. Soc. Am. 38 (1948) 448–457.

[65] M. Fernández-García, A. Martínez-Arias, J.C. Hanson, J.A. Rodriguez, Chem. Rev. 104 (2004) 4063–4105.
[66] D.A. Shirley, Phys. Rev. B 5 (1972) 4709–4714.
[67] M.L. Satuf, R.J. Brandi, A.E. Cassano, O.M. Alfano, Ind. Eng. Chem. Res. 44 (2005) 6643–6649.
[68] R. Siegel, J.R. Howell, Thermal Radiation Heat Transfer, fourth ed., Hemisphere Publishing Corp., Bristol, PA, 2002.
[69] M.I. Cabrera, O.M. Alfano, A.E. Cassano, J. Phys. Chem. 100 (1996) 20043–20050.
[70] R.L. Romero, O.M. Alfano, A.E. Cassano, Ind. Eng. Chem. Res. 36 (1997) 3095–3109.
[71] C.S. Zalazar, M.D. Lambas, C.A. Martin, R.J. Brandi, O.M. Alfano, A.E. Cassano, J. Chem Eng, (2005) 67–81.
[72] J.J. Duderstadt, W.R. Martin, Transport Theory, Wiley, New York, 1979.
[73] C.D. Wagner, W.M. Riggs, L.E. Davis, J.F. Moulder, in: G.E. Muilenber (Ed.), Handbook of X-ray Photoemission Spectra, Perkin-Elmer, Minnesota, 1976.
[74] E.L. Lee, E.I. Wachs, J. Phys. Chem. C 111 (2007) 14410–14425.
[75] A. Atanacio, T. Bak, J. Nowotny, J. Phys. Chem. C 118 (2014) 11174–11185.
[76] A.A.S. Karakoti, J.E.S. King, A. Vincet, S. Seal, Appl. Catal. A 388 (2010) 262–271.
[77] Z. Wei, E. Kowalska, K. Wang, C. Colbeau-Justin, B. Ohtani, Catal. Today 280 (2017) 29–36.
[78] M.J. Muñoz-Batista, A. Kubacka, M. Fernández-García, ACS Catal. 4 (2014) 4277–4288.
[79] A.L. Luna, E. Novosetheva, E. Louran, B. Othani, M. Avaluzuela, H. Renita, J.C. Colbaeu-Justin, Appl. Catal. B 191 (2016) 18–28.
[80] S. Escobedo Salas, B. Serrano Rosales, H. de Lasa, Appl. Catal. B 140-141 (2013) 523–536.
[81] J.F. Guayaquil-Sosa, B. Serrano Rosales, P.J. Valadés-Pelayo, S. Escobedo, H. de Lasa, Appl. Catal. B 211 (2017) 337–348, http://dx.doi.org/10.1016/j.apcatb.2017.04.029.
[82] J. Liu, Y. Liu, N. Liu, Y. Han, X. Zhang, H. Huang, Y. Lifshitz, S.-T. Lee, J. Zhong, Z. Kang, Science 347 (2015) 970–974.
[83] G. Box, D. Behnken, Some new three level designs for the study of quantitative variables, Technometrics 2 (1960) 455–475.
[84] E. Pulido Melián, J.A. Ortega Méndez, D.E. Santiago, J.M. Doña Rodríguez, O. González Díaz, J. Photochem. Photobiol. A 312 (2015) 45–54.
[85] G. Wua, T. Chen, W. Su, G. Zhou, X. Zong, Z. Lei, C. Li, G. Wu, Int. J. Hydr. Energy 33 (2008) 3841–3848.
[86] R.J. Brandi, G. Rintoul, O.M. Alfano, A.E. Cassano, Catal. Today 76 (2002) 161–166.
[87] T. Tachikawa, T. Majima, J. Am. Chem. Soc. 131 (2009) 8485–8494.
[88] C.C. Mercado, Z. Seeley, A. Bandyopadhyay, Z. Bose, J.L. McHale, ACS Applied Mater. Interf. 3 (2011) 228–235.
[89] M.J. Muñoz-Batista, A. Kubacka, M. Fernández-García, Catal. Sci. Technol. 4 (2014) 2006–2015.
[90] M.A. Grela, M.E.J. Coronel, A.J. Colussi, J. Phys. Chem. 100 (1996) 16940–16948.
[91] E.G. Janzen, N. Sankuratry, Y. Kotake, J. Magn. Reson. 111 (1996) 254–263.
[92] A. Kubacka, M.J. Muñoz-Batista, M. Ferrer, M. Fernández-García, Appl. Catal. B 140-141 (2013) 680–690.
[93] Q. Chen, H. Shi, W. Shi, Y. Xu, D. Wu, Catal. Sci. Technol. 2 (2012) 1213–1220.
[94] W. He, H. Jia, W.G. Wamer, Z. Zheng, P. Li, J.H. Callahan, J.-J. Jin, J. Catal, (2014) 97–105.